GIFAD for He/KCl(001). Structure in the pattern for ⟨110⟩ incidence as a measure of the projectile-cation interaction

G.A. Bocan[a,*,1], M.S. Gravielle[b,1]

[a] Centro Atómico Bariloche, Av. Bustillo 9500, 8400 S.C. de Bariloche, Argentina
[b] Instituto de Astronomía y Física del Espacio (IAFE, CONICET-UBA), Casilla de Correo 67, Sucursal 28, C1428EGA Buenos Aires, Argentina

ARTICLE INFO

ABSTRACT

In this article we address grazing incidence fast atom diffraction (GIFAD) for the He/KCl(001) system, for which a systematic experimental study was recently reported [E. Meyer, Ph.D dissertation, Humboldt-Universität, Berlin, Germany, 2015]. Our theoretical model is built from a projectile-surface interaction obtained from Density Functional Theory (DFT) calculations and the Surface Initial-Value Representation (SIVR), which is a semi-quantum approach to describe the scattering process. For incidence along the ⟨100⟩ and ⟨110⟩ directions, we present and discuss the main features of our interaction potential, the dependence of the rainbow angle with the impact energy normal to the surface, and the simulated GIFAD patterns, which reproduce the main aspects of the reported experimental charts. The features of the diffraction charts for He/KCl(001) are related to the averaged equipotential curves of the system and a comparison is established with the case of He/LiF(001). The marked differences observed for ⟨110⟩ incidence are explained as due to the much larger size of the K^+ ion relative to that of Li^+.

1. Introduction

Grazing incidence fast atom diffraction (GIFAD) [1,2] is being rapidly incorporated to the set of surface analysis techniques. It shares with reflection high-energy electron diffraction (RHEED) the grazing incidence geometry, and complements thermal energy atom scattering (TEAS) [3] in the keV range just as RHEED does with low energy electron diffraction (LEED). GIFAD was first reported in 2007 [1,2] and its potential for nondestructive surface characterization was very early foreseen [4,5]. Furthermore, the extreme sensitivity of GIFAD to the projectile-surface interaction has positioned this technique as a powerful tool for probing potential energy surfaces (PES).

Incidence along or very close to high-symmetry directions is a requirement for the observation of non-specular scattering [6,7]. The GIFAD phenomenon takes place when atomic projectiles in the keV energy range grazingly impinge on a crystal surface along a low-index crystallographic direction. The scattering thus proceeds under axial surface channeling conditions [8]. The fast motion along the channel is, on a first approach, sensitive only to the periodic-PES average in this direction [9]. Hence, the associated energy $E_\parallel$ is essentially conserved, and motions parallel and perpendicular to the channel get decoupled from each other. The scattering process can then be projected into the

plane normal to the channeling direction, with an associated energy $E_\perp$ in a hyperthermal up to eV energy regime and a perpendicular De Broglie wavelength of the order of the interatomic spacing. Bragg diffraction out of the specular plane occurs whenever the transverse momentum transfer coincides with a reciprocal lattice vector. Such a transverse momentum exchange had already been proposed by Farías et al. [10] in 2004 to explain their observations for the scattering of H_2/Pd(111), at off-normal incidence with energies $E_i < 1$ eV.

The GIFAD pattern arises from the combination of two kinds of interference: a) interchannel interference, originated from the periodic array of channels, giving the Bragg peaks and b) intrachannel interference, originated from the corrugation of the interaction potential within a given channel, giving the rainbow peak as well as the supernumerary rainbows [11]. The result on the detection plane is typically a sequence of Bragg peaks whose intensities are modulated by the underlying intrachannel interference [11,12].

Although GIFAD has already been observed for a wide variety of surfaces, including semiconductors [4,13], metals [14,15], adsorbate-covered metals [5], ultra-thin films [16], organic molecules on metal substrates [17], etc., He/LiF(001) remains the benchmark system as the wide band-gap insulator character of LiF(001) together with the closed-shell electronic structure of He result in an efficient suppression of

electronic excitations [18]. Similar systems such as He/NaCl(001) [2], H/LiF(001) [1,2,19] or H/NaCl(001) [2] were examined as well in the early GIFAD experimental works, but so far they have not been as extensively studied [20–22]. In the present article we will address the ^{4}He/KCl(001) system, the choice being strongly motivated by the experimental GIFAD diffraction charts recently reported by Meyer [23]. This system had previously been the subject of a rainbow-scattering theo-experimental study by Specht et al. [24,25], who analyzed the effect of the rumpling on the rainbow angle.

Our theoretical model for GIFAD is built from a high-precision interaction potential built from Density Functional Theory (DFT) calculations and a semi-quantum representation of the scattering process called the surface initial-value representation (SIVR) [26]. In this contribution we will use this model to simulate GIFAD for He/KCl(001). The focus of our analysis will be on i) the adequacy of our potential to reproduce the experimental GIFAD patterns [23]; and ii) the qualitatively different structure of the He/KCl(001) GIFAD pattern relative to that of He/LiF(001), particularly for incidence along the ⟨110⟩ direction.

We will show that simulated GIFAD patterns give a good accord with experiments for $\lambda_\perp \leqslant 0.6$ Å. Also we will explain the very different structure of the ⟨110⟩ chart, when compared with that of He/LiF(001), as arising from the much larger size of the K$^+$ cation relative to that of Li$^+$, resulting in the early presence of a double-well on the averaged equipotential curves. Noteworthily, a double-well shape had been predicted for H/LiF(001) by Rousseau et al. [19] based on the specific GIFAD patterns for that system. In a recent publication, we indeed observed that feature for H→ ⟨110⟩ LiF(001) [22].

This article is organized as follows: In Section 2 we briefly introduce the SIVR method and the interaction potential; in Section 3 we discuss the results concerning i) the features of the interaction potential, ii) the rainbow angle and iii) simulated diffraction charts. A comparison with He/LiF(001) is established in order to gain some insight into the nature of the projectile-cation interaction and how it affects the GIFAD pattern for incidence along the ⟨110⟩ direction. Finally in Section 4 we present our conclusions.

2. Theoretical model

2.1. Scattering process

We treat the scattering dynamics of He atoms grazingly colliding with the KCl(001) surface by means of the SIVR model [26,27]. This semi-quantum approach is based on the Initial Value Representation (IVR) method by Miller [28], which represents a practical way of introducing quantum effects, such as interferences and classical forbidden processes, in classical dynamics simulations [29]. The basic idea of IVR is, within the Feynman path integral formulation, to replace the full-quantum time evolution operator by the Van Vleck propagator in terms of classical trajectories with different initial conditions. This evolution operator is then evaluated numerically without any further approximation. The SIVR model uses the IVR time evolution operator in the frame of a time-dependent distorted-wave formalism. In accord with a full-quantum treatment, a smooth maximum is obtained at the classical rainbow angle, which exponentially decays on the classical forbidden region. The SIVR method provides an appropriate description of GIFAD patterns along the whole angular range and can be considered as an attractive alternative to quantum wave packet propagations, offering a clear representation of the main mechanisms of the GIFAD process. The interested reader can find a more detailed discussion of the SIVR model in Refs. [22,26,27].

Regarding the present calculation, notice that SIVR projectile distributions are sensitive to the size of the surface region that is coherently illuminated by the incident beam, and this size depends on the collimating setup [27,30,31]. In this work we assume a coherently illuminated square region covering two equivalent parallel channels of the surface lattice, i.e., we use transverse coherent lengths $\sigma_x = \sigma_y = 2a_y$

in Eq. (7) from Ref. [31], where a_y is the half-width of the incidence channel. The angular dispersion was derived from these parameters by using Eq. (10) from Ref. [31] considering an impact energy $E = 2$ keV. The resulting azimuthal divergence of the incident beam ranges between 0.01 and 0.02 deg, being in accord with the experimental value that is smaller than 0.03 deg [25]. In connection with this it should be mentioned that GIFAD experiments also involve inelastic processes [32], which are not included in our model and might affect the spectra. In addition, the starting point of the classical projectile trajectories was chosen at the normal position $Z_o = 1.4\ a$ (a is the lattice constant) relative to the surface, thus ensuring a negligible projectile-surface interaction.

2.2. Projectile-surface potential

The He-KCl(001) potential was obtained from DFT calculations, performed with the QUANTUM ESPRESSO code [33]. The procedure was analogous to the one discussed for H-LiF(001) in Ref. [22]. In this section we briefly present its main features.

The PES is three-dimensional (3D) and is built out of a selection of 6 high-symmetry (X_i, Y_i) configurations and 20 Z_i values ($Z = 0$ falls on the topmost Cl layer), by means of a three-dimensional interpolation technique, which makes use of cubic splines and the corrugation reducing procedure (CRP) [34].

For the DFT calculations, we use projector augmented-wave (PAW) pseudopotentials [35,36] to describe the electron-core interaction, while for the exchange–correlation functional we consider the generalized gradient approximation (GGA), with the Perdew-Burke-Ernzerhof (PBE) functional [37]. Thus, we will hereafter refer to the resulting interaction potential as a PAW-PBE PES.

The DFT calculations are performed with an energy cutoff in the plane-wave expansion of 80 Ryd for the wave functions and 320 Ryd for the charge density and potential. A $2 \times 2 \times 1$ Monkhorst–Pack grid of special k-points is used for the Brioullin-zone integration. The KCl lattice constant is $a = 6.381$ Å, slightly higher than the experimental value of 6.28 Å [38].

We represent the KCl(001) surface by means of the supercell-slab scheme. The supercell consists of a $\sqrt{2} \times \sqrt{2}$ surface cell, a six-layer slab and a vacuum distance of $6d = 3\frac{a}{2} \sim 9.6$ Å. The relaxed surface equilibrium geometry presents a *rumpling*, defined as the half-distance between relaxed Cl and K planes. For the topmost Cl and K planes, we get a rumpling of + 0.025 Å, with Cl atoms moving outward and K atoms moving inward. This value is consistent with LEED experiments which yield a rumpling of 0.03 ± 0.05 Å [38] and compares very well with Specht's 0.03 Å [24], obtained from a vdW-D2 calculation (PBE plus semiempirical dispersion corrections [39]).

The geometry of GIFAD for He/KCl(001) as well as the channeling directions ⟨110⟩ and ⟨100⟩ are illustrated in Fig. 1.

3. Results and discussion

3.1. The potential energy surface

GIFAD is extremely sensitive to the projectile-surface interaction, particularly to the profile and corrugation of the PES near the reflection region. Our PES is 3D and no dimension reduction is made during the dynamics. However, the fast motion of the projectile along the channel is in fact mainly ruled by the average interaction in this direction and thus we will discuss the PES features in these terms.

In Fig. 2a and b we consider the energy averages respectively along the ⟨100⟩ and ⟨110⟩ channels, and depict equipotential contours across them. Across a ⟨100⟩ channel, the equipotential curves have only one maximum at the border of the channel, corresponding to the rows of alternating Cl$^-$ and K$^+$ ions. In contrast, across a ⟨110⟩ channel the equipotential curves have local maxima both at the border and at the middle of the channel, respectively corresponding to the rows of Cl$^-$
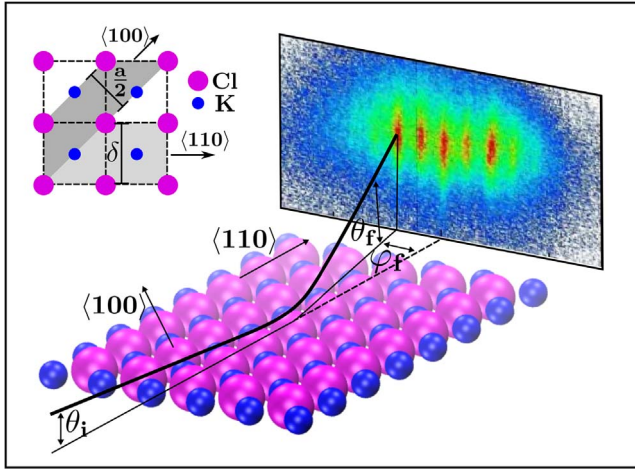
Fig. 1. Sketch for GIFAD from a KCl(001) surface including relevant angles and channeling directions. Inset: Detail of the (001) surface depicting the widths $\frac{a}{2}$ and $\delta = \frac{a}{\sqrt{2}}$, respectively corresponding to channels $\langle 100 \rangle$ and $\langle 110 \rangle$.

and K^+ ions (see inset of Fig. 1). These results can be compared with those reported by Specht et al. [24], also shown in Fig. 2. An almost perfect match is obtained for $E_\perp > 0.2$ eV, while the slightly more attractive character of Specht's equipotential curves for $E_\perp = 0.075$ eV is due to the inclusion of semiempirical Van der Waals interactions in those calculations.

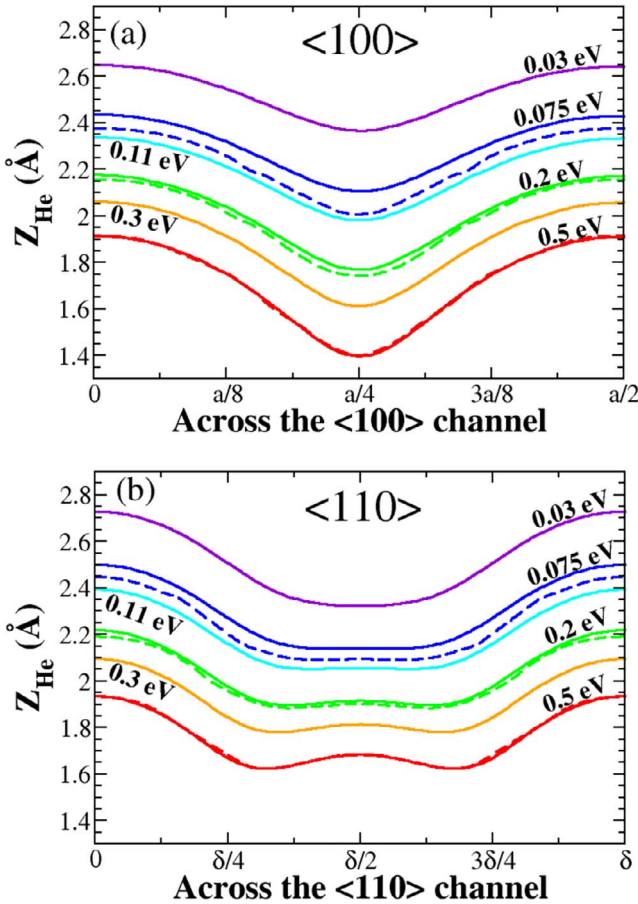The corrugation $\Delta Z = Z_{max} - Z_{min}$ of the equipotential curve, as

Fig. 2. Equipotential contours averaged along the incidence channel. a) Incidence along $\langle 100 \rangle$ direction. b) Incidence along $\langle 110 \rangle$ direction. δ and $a/2$ correspond to the respective channel widths as depicted in Fig. 1. Solid lines: This work. Dashed lines: Calculations by Specht, extracted from Ref. [24].
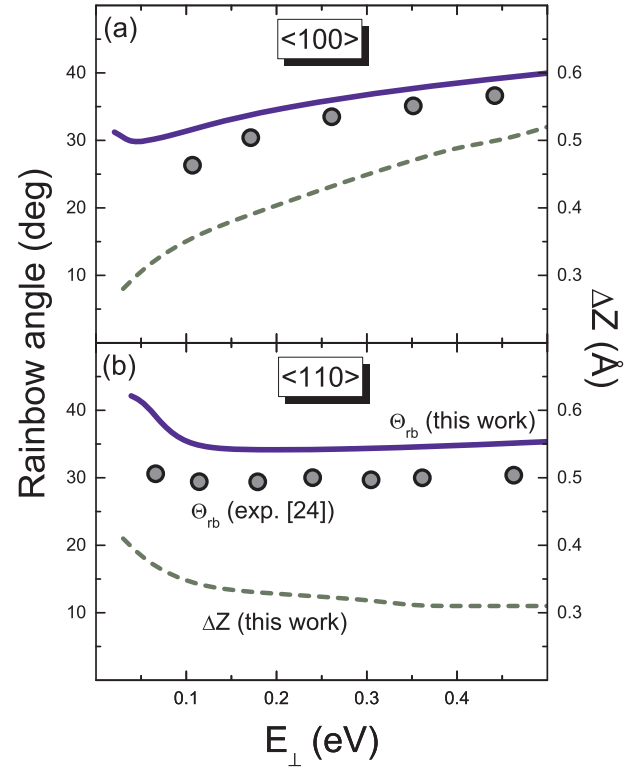

Fig. 3. Rainbow deflection angle measured on the detection plane (scale on the left axis), and corrugation at the reflection region (scale on the right axis) as functions of the perpendicular energy $E_\perp$ of the projectile. a) Incidence along $\langle 100 \rangle$ direction. b) Incidence along $\langle 110 \rangle$ direction. Grey filled circles: Rainbow angle, exps. by Specht et al. [24]. Blue line: Rainbow angle, this work. Green dashed line: Corrugation, this work.

well as the way it evolves with $E_\perp$, are key features of the PES, with marked effects on the GIFAD pattern. In Fig. 3 we show for each channel the corrugation as a function of $E_\perp$. We note that for a $\langle 100 \rangle$ channel higher $E_\perp$ leads to higher corrugation, while for a $\langle 110 \rangle$ channel the corrugation initially decreases with increasing $E_\perp$, becoming approximately constant for $E_\perp \geqslant 0.15$ eV.

At this point it is worth comparing the mentioned features of the He/KCl(001) PAW-PBE PES with those reported for He/LiF(001). Potential energy surfaces for He/LiF(001) within the local density approximation (LDA) have been reported by Pruneda [12] and Wirtz [40]. The equipotential curves for He/KCl(001) across $\langle 100 \rangle$ present a cosine-like character, similar to those of He/LiF(001) (see analysis in Section 4.1 in Ref. [19]). Across $\langle 110 \rangle$ however, the equipotential curves of He/LiF(001) and He/KCl(001) are qualitatively different from each other. The double well observed for He/KCl(001) is also obtained for He/LiF (001) but the latter arises at much higher energies ($E_\perp > 2$ eV [7,8,40,41]). In the energy range $E_\perp \lesssim 2$ eV a minimum along the row of Li^+ ions is obtained instead. The origin of the early double-well obtained for He $\rightarrow \langle 110 \rangle$ KCl(001) is the different effective size of the K^+ and Li^+ ions. Both cations have a closed shell character with comparatively sharp repulsion, but K^+, isoelectronic with Ar, is significantly larger than Li^+, isoelectronic with He [42]. This difference will have strong effects on the respective structures of the diffraction patterns as we will see and further discuss in Section 3.3. Regarding the corrugation across the $\langle 110 \rangle$ channel, it is interesting to note that for increasing $E_\perp$ an almost constant behavior is obtained for both He/LiF (001) [8,12,43] and He/KCl(001), despite the differences just discussed concerning the equipotential curves. This curious similarity is the result of how the interplay between the He-cation and the He-anion repulsion varies with $E_\perp$ for each system.

3.2. The rainbow angle

The corrugation of the average PES across the channeling direction gives rise to an extreme in the angular deflection, called the *rainbow angle*. In this angular position an enhanced flux of scattered projectiles, the rainbow peak, is observed [3]. The position of the rainbow peak can be obtained from our GIFAD simulation by considering impinging projectiles along a single channel so as to turn off interchannel interference. In Fig. 3 we show the rainbow angle as a function of the projectile perpendicular energy $E_\perp$ for both $\langle 100 \rangle$ and $\langle 110 \rangle$ channels and compare it with the experimental values reported by Specht et al. [24]. Our theoretical rainbow angles are in fairly good agreement with the experiment. For $\langle 100 \rangle$ we correctly reproduce the experimental curve, monotonously increasing for $E_\perp > 0.1$ eV. Our rainbow angles fall slightly above the experimental ones, about 10% for 0.2 eV, with an improving accord for higher $E_\perp$ values. Similarly, for $\langle 110 \rangle$ we reproduce the constant experimental rainbow for $E_\perp > 0.1$ eV, though in this case our values are about 17% higher than experiments. Another interesting aspect of the rainbow angle, illustrated in Fig. 3, is how the trend of its dependence with $E_\perp$ can be traced back to that of the corrugation. Note that the equipotential curves shown in Fig. 2 present either a single-well or a double-well where the height of the central local maximum is much smaller than the corrugation. In these conditions, the maximum slope of an equipotential curve, which mainly determines the angular position of the rainbow Θ_{rb}, is closely related to its corrugation. What is more, for $\langle 110 \rangle$ incidence, the approximately constant behavior of Θ_{rb} with $E_\perp$, observed for both He/KCl(001) (Fig. 3b and Ref. [24]) and He/LiF (001) [12], may be interpreted as a direct consequence of the presence of the cationic and anionic rows along the channels. In fact, even before the emergence of the double well, the He-cation and He-anion interactions evolve with $E_\perp$ in such a fashion that the magnitude of the maximum slope is not much altered. In contrast, the configuration of the surface atoms for $\langle 100 \rangle$ incidence yields a corrugation and a maximum slope that increase with $E_\perp$ as consequently does the rainbow angle.

3.3. Diffraction charts

In this section we will present and discuss the diffraction charts for the ^{4}He/KCl(001) system. A diffraction chart captures in a single graph the projected intensity dependence on both the deflection angle Θ and the $E_\perp$ value, though the latter is usually portrayed in terms of $\lambda_\perp = h/\sqrt{2m E_\perp}$ (see Table 1 for $\lambda_\perp \rightarrow E_\perp$ conversion results). The deflection angle is defined on the detection plane as $\Theta = arctg(\varphi_f/\theta_f)$, where θ_f and φ_f are the polar and azimuthal dispersion angles, respectively (see Fig. 1). The comparison of simulated and experimental charts provides a global perspective of the performance of the theoretical model, allowing for an analysis of its suitability for the different angular and/or $E_\perp$ regions.

The theoretical charts for ^{4}He/KCl(001) are shown in the bottom panels of Fig. 4, together with the experimental ones reported by Meyer [23], displayed in the top panels. For every $\lambda_\perp$ value the angular positions of observed maxima follow from the Bragg condition

Table 1
Conversion to $E_\perp$, for ^{4}He, from a set of $\lambda_\perp$ values in the region shown in Fig. 4.

$\lambda_\perp$ (Å)	$E_\perp$ for ^{4}He (eV)
0.30	0.229
0.35	0.168
0.40	0.129
0.45	0.102
0.50	0.082
0.55	0.068
0.60	0.057

$n \lambda_\perp = D \sin(\Theta_n)$, where D is the periodicity of the channel array, $\lambda_\perp$ is the de Broglie wavelength associated to $E_\perp$, n is the interference order and Θ_n is the deflection angle.

For incidence along $\langle 100 \rangle$, our simulation very well reproduces the experiment. Particularly the high intensities of the peaks near the rainbow angle and the Θ-$\lambda_\perp$ position and relative intensities of the Bragg peaks. The higher intensities we obtain near the rainbow region, compared to the experiments, can probably be due to the neglect of thermal vibration and inelastic contributions in our calculations. Both effects are expected to affect experimental GIFAD patterns [32,44]. In fact, theoretical studies for Ne/LiF(001) elastic scattering suggest that thermal vibrations of lattice atoms might reduce the intensity of rainbow maxima and widen all Bragg peaks [45].

The chart for incidence along $\langle 110 \rangle$ does not present a structure as regular as the one observed for $\langle 100 \rangle$. Its main features prove however more difficult to capture. From a comparison with the experiment, we observe that our simulation reproduces the central structure though somehow shifted to higher $\lambda_\perp$. Also, the intensity of the simulated peaks near the rainbow region is overly high. These features could all probably be traced to a slight overestimation of the surface rumpling, to which this direction is highly sensitive, and a resulting slightly overestimated corrugation. In fact a smaller rumpling would: i) give a smaller rainbow angle in better accord with experiments (particularly for $\langle 110 \rangle$), ii) shift down the $\langle 110 \rangle$ chart without much affecting the $\langle 100 \rangle$ chart, and iii) maybe reduce the intensity near the $\langle 110 \rangle$ rainbow region. Concerning point ii) note that a reduced rumpling would result in a shift of the chart to higher $E_\perp$ values (see the dependence on $E_\perp$ of the corrugation in Fig. 3), that is to lower $\lambda_\perp$ values and therefore to a better quantitative accord with experiments. The slight overestimation of the corrugation could also be related to the polarization, which has been shown to affect the GIFAD patterns [46] for He $\rightarrow \langle 110 \rangle$LiF(001). A thorough study regarding these issues is currently being addressed for a forthcoming article.

Despite the quantitative details just discussed, our calculations for ^{4}He/KCl(001) do capture the complex structure of the $\langle 110 \rangle$ chart, which strikingly contrasts with the much more regular $\langle 100 \rangle$ one, but also with the well-documented quasi-periodic behavior of the $\langle 110 \rangle$ GIFAD patterns for He/LiF(001) [1,2,7,8,12,19,40,41,47]. The reason for this lies on the equipotential contours in Fig. 2b, the analysis of which we resume here. The double-well profile across the $\langle 110 \rangle$ channel for He/KCl(001) gives rise to two separated axial channels within the unit cell, leading to Young-type interference as described by Seifert-Winter for He on O-covered Mo(112) [48]. Within a semiclassical description this means that for He/KCl(001) up to four different trajectories from a single channel may contribute to some deflection angles, while for He/LiF(001) it was only two (see Fig. 1 in Ref. [11]). This extra contribution results in additional minima in the intensity profile, which contribute to the shattering of the modulating supernumerary rainbow peaks, thus qualitatively affecting the GIFAD pattern.

Summing up, the larger size of the K^+ cation relative to the more compact nature of Li^+ leads to an early emergence of local maxima in the equipotential contours of He/KCl(001), when averaged along the $\langle 110 \rangle$ direction. These maxima sit on top of the averaged cationic rows and they do arise as well for He/LiF(001) but at much higher $E_\perp$ values. The resulting double-well structure of the average potential across the $\langle 110 \rangle$ for He/KCl(001) adds a new form factor to the GIFAD intensity distribution. This Young-type interference within the channel greatly alters the structure of the GIFAD pattern for this channeling direction making it more complex and much richer.

4. Conclusions

In the present article we have addressed GIFAD for He/KCl(001) with the focus on the adequacy of a PAW-PBE PES and the origin of the particular structure of its diffraction chart for incidence along the $\langle 110 \rangle$ direction. In this section we summarize our conclusions.
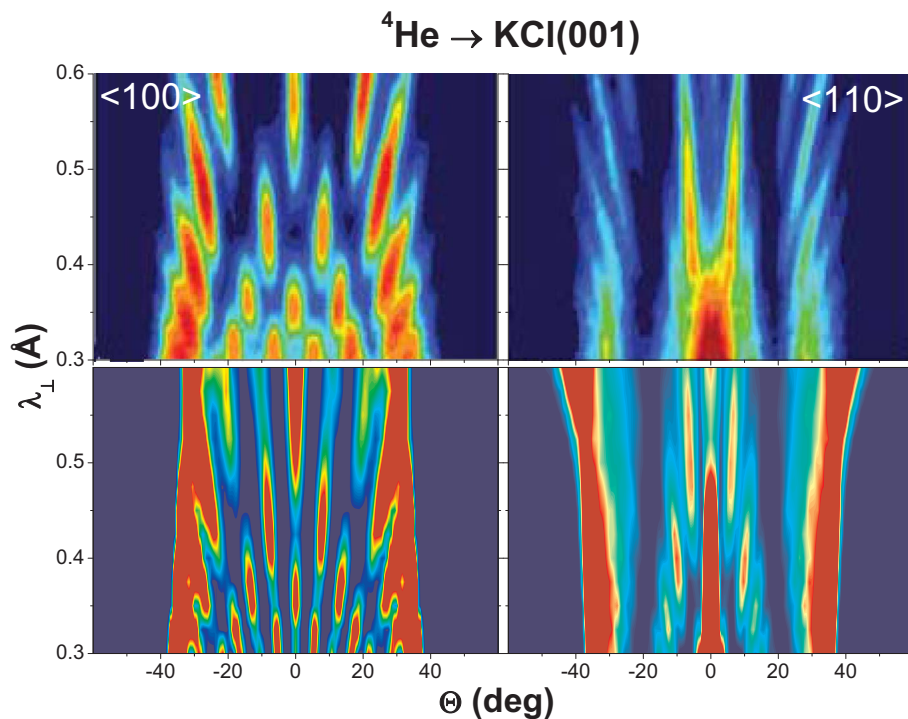
^{4}He → KCl(001)

Fig. 4. Diffraction chart for the ^{4}He/KCl(001) system, in terms of $\lambda_\perp$ and the deflection angle on the detection plane. TOP charts: Experiments by Meyer [23] for incidence along the ⟨100⟩ channel (LEFT) and ⟨110⟩ channel (RIGHT). BOTTOM charts: Our respective simulations.

The PAW-PBE PES performed well in describing the main features of the GIFAD pattern for both incidence directions. Slight quantitative differences with experiments particularly for ⟨110⟩ incidence, are probably due to the high sensitivity of GIFAD to the rumpling. The accord with experiments might improve by including thermal vibrations or inelastic processes to the dynamics and/or dispersion corrections to the PES.

We have explained the structure of the ⟨110⟩ chart, very different from that of He/LiF(001), as arising from the larger size of the K^+ cation compared with that of Li^+. The consequent early presence of a local maximum on the equipotential curves, when averaged along the row of K^+ ions, which is not observed in He/LiF(001) for $E_\perp < 2$ eV, yields Young-type interference within the channel and the result is an important change in the structure in the GIFAD pattern. Moreover, the progressive appearance of the double well in this system makes it a most interesting and appealing candidate to study the transition from two-trajectory interference to four-trajectory interference within a single channel.

The results in this article are intended as a first report on a currently ongoing investigation, aimed to gain insight into the nature of the surface-projectile interaction in GIFAD from the comparison of the well-known He/LiF(001) system with similar ones such as H/LiF(001), He/KCl(001) and H/KCl(001).

Acknowledgments

References

[1] A. Schüller, S. Wethekam, H. Winter, Diffraction of fast atomic projectiles during grazing scattering from a LiF(001) surface, Phys. Rev. Lett. 98 (2007) 016103.

[2] P. Rousseau, H. Khemliche, A.G. Borisov, P. Roncin, Quantum scattering of fast atoms and molecules on surfaces, Phys. Rev. Lett. 98 (2007) 016104.

[3] D. Faŕas, K.-H. Rieder, Atomic beam diffraction from solid surfaces, Rep. Prog. Phys. 61 (1998) 1575–1664.

[4] H. Khemliche, P. Rousseau, P. Roncin, V.H. Etgens, F. Finocchi, Grazing incidence fast atom diffraction: an innovative approach to surface structure analysis, Appl. Phys. Lett. 95 (2009) 151901.

[5] A. Schüller, M. Busch, S. Wethekam, H. Winter, Fast atom diffraction from superstructures on a Fe(110) surface, Phys. Rev. Lett. 102 (2009) 017602.

[6] A. Ruiz, J.P. Palao, E. Heller, Classical and quantum analysis of quasiresonance in grazing atom-surface collisions, Phys. Rev. A 79 (2009) 052901.

[7] A. Schüller, H. Winter, Difraction of fast atoms under axial surface channeling conditions, Nucl. Instr. Methodss. Res. B 267 (2009) 628–633.

[8] H. Winter, A. Schüller, Fast Atom Diffraction during Grazing Incidence from Surfaces, Prog. Surf. Sci. 86 (2011) 169–221.

[9] A. Zugarramurdi, A.G. Borisov, Transition from fast to slow atom diffraction, Phys. Rev. A 86 (2012) 062903.

[10] D. Faŕas, C. Diz, P. Nieto, A. Salin, F. Martĺn, Pronounced out-of-plane diffraction of H2 molecules from a Pd(111) surface, Chem. Phys. Lett. 390 (2004) 250–255.

[11] A. Schüller, H. Winter, Supernumerary rainbows in the angular distribution of scattered projectiles for grazing collisions of fast atoms with a LiF(001) surface, Phys. Rev. Lett. 100 (2008) 097602.

[12] A. Schüller, H. Winter, M.S. Gravielle, J.M. Pruneda, J.E. Miraglia, He-LiF surface interaction potential from fast atom diffraction, Phys. Rev. A 80 (2009) 062903.

[13] M. Debiossac, A. Zugarramurdi, H. Khemliche, P. Roncin, A.G. Borisov, A. Momeni, P. Atkinson, M. Eddrief, F. Finocchi, V.H. Etgens, Combined experimental and theoretical study of fast atom diffraction on the $\beta_2(2 \times 4)$ reconstructed GaAs(001) surface, Phys. Rev. B 90 (2014) 155308.

[14] N. Bundaleski, H. Khemliche, P. Soulisse, P. Roncin, Grazing incidence diffraction of kev helium atoms on a Ag(110) surface, Phys. Rev. Lett. 101 (2008) 177601.

[15] M. Busch, A. Schüller, S. Wethekam, H. Winter, Fast atom diffraction at metal surface, Surf. Sci. 603 (2009) L23.

[16] J. Seifert, A. Schüller, H. Winter, R. Włodarczyk, J. Sauer, M. Sierka, Diffraction of fast atoms during grazing scattering from the surface of an ultrathin silica film on Mo(112), Phys. Rev. B 82 (2010) 035436.

[17] J. Seifert, M. Busch, E. Meyer, H. Winter, Surface structure of alanine on Cu(110) studied by fast atom diffraction, Phys. Rev. Lett. 111 (2013) 137601.

[18] F. Aigner, N. Simonović, B. Solleder, L. Wirtz, J. Burgdörfer, Suppression of decoherence in fast-atom diffraction at surfaces, Phys. Rev. Lett. 101 (2008) 253201.

[19] P. Rousseau, H. Khemliche, N. Bundaleski, P. Soulisse, A. Momeni, P. Roncin, Surface analysis with grazing incidence fast atom diffraction (GIFAD), J. Phys. Conf. Ser. 133 (2008) 012013.

[20] A.S. Muzas, F. Martin, C. Díaz, Scattering of H(D) from LiF(100) under Fast Grazing Incidence Conditions: To What Extent is Classical Dynamics a Useful Tool? Nucl. Instrum. Methods Phys. Res. B 354 (2015) 9–15.

[21] A.S. Muzas, F. Gatti, F. Martin, C. Díaz, Diffraction of H from LiF(001): From slow normal incidence to fast grazing incidence, Nucl. Instrum. Methods Phys. Res. B 382 (2016) 49–53.

[22] G.A. Bocan, J.D. Fuhr, M.S. Gravielle, van der Waals effects on grazing-incidence fast-atom diffraction for H on LiF(001), Phys. Rev. A 94 (2016) 022711.

[23] E. Meyer, Strukturuntersuchungen an Oxidkristalloberflächen mittels der streifenden Streuung schneller Atome, Habilitattionsschrift PhD dissertation, Humboldt Universität Berlin, Germany, 2015, http://dx.doi.org/10.18452/17442.

[24] U. Specht, M. Busch, J. Seifert, H. Winter, K. Gärtner, R. Włodarczyk, M. Sierka, J. Sauer, Classical and quantum mechanical rainbow scattering of fast He atoms from a KCl(001) surface, Nucl. Instrum. Methods Phys. Res. B 269 (2011) 799–803.

[25] U. Specht, M. Busch, J. Seifert, A. Schüller, H. Winter, K. Gärtner, R. Włodarczyk, M. Sierka, J. Sauer, Rainbow scattering under axial surface channeling from a KCl (001) surface, Phys. Rev. B 84 (2011) 125440.

[26] M.S. Gravielle, J.E. Miraglia, Semiquantum approach for fast atom diffraction: solving the rainbow divergence, Phys. Rev. A 90 (2014) 052718.

[27] M.S. Gravielle, J.E. Miraglia, Influence of beam collimation on fast-atom diffraction studied via a semiquantum approach, Phys. Rev. A 92 (2015) 062709.

[28] W.H. Miller, Classical S matrix: numerical application to inelastic collisions, J. Chem. Phys. 53 (1970) 3578–3587.

[29] W.H. Miller, The semiclassical initial value representation: a potentially practical way for adding quantum effects to classical molecular dynamics simulations, J. Phys. Chem A 105 (2001) 2942–2955.

[30] J. Seifert, J. Lienemann, A. Schüller, H. Winter, Studies on coherence and decoherence in Fast Atom Diffraction, Nucl. Instrum. Methods Phys. Res. B 350 (2015) 99–105.

[31] M.S. Gravielle, J.E. Miraglia, Single- and double-slit collimating effects on fast-atom diffraction spectra, Nucl. Instrum. Methods Phys. Res. B 382 (2016) 42–48.

[32] P. Roncin, M. Debiossac, Elastic and inelastic diffraction of fast atoms, Debye-Waller factor, and Mössbauer-Lamb-Dicke regime, Phys. Rev. B 96 (2017) 035415.

[33] P. Giannozzi, S. Baroni, N. Bonini, M. Calandra, R. Car, C. Cavazzoni, D. Ceresoli, G.L. Chiarotti, M. Cococcioni, I. Dabo, A.D. Corso, S. Fabris, G. Fratesi, S. de Gironcoli, R. Gebauer, U. Gerstmann, C. Gougoussis, A. Kokalj, M. Lazzeri, L. Martin-Samos, N. Marzari, F. Mauri, R. Mazzarello, S. Paolini, A. Pasquarello, L. Paulatto, C. Sbraccia, S. Scandolo, G. Sclauzero, A.P. Seitsonen, A. Smogunov, P. Umari, R.M. Wentzcovitch, QUANTUM ESPRESSO: a modular and open-source software project for quantum simulations of materials, J. Phys.: Cond. Matter. 21 (2009) 395502.

[34] H.F. Busnengo, A. Salin, W. Dong, Representation of the 6D potential energy surface for a diatomic molecule near a solid surface, J. Chem. Phys. 112 (2000) 7641–7651.

[35] G. Kreese, D. Joubert, From ultrasoft pseudopotentials to the projector augmented-wave method, Phys. Rev. B 59 (1999) 1758.

[36] He.pbe-kjpawpsl.1.0.0.UPF, K.pbe-spn-kjpawpsl.1.0.0.UPF, Cl.pbe-n-kjpawpsl.1.0.0.UPF, www.quantum-espresso.org.

[37] J.P. Perdew, K. Burke, M. Ernzerhof, Generalized gradient approximation made simple, Phys. Rev. Lett. 77 (1996) 3865.

[38] J. Vogt, H. Weiss, The structure of NaCl(100) and KCl(100) single crystal surfaces: a tensor low energy electron diffraction analysis, Surf. Sci. 491 (2001) 155–168.

[39] S. Grimme, Semiempirical GGA-type density functional constructed with a long-range dispersion correction, J. Comput. Chem. 27 (2006) 1787–1799.

[40] A. Schüller, S. Wethekam, D. Blauth, H. Winter, F. Aigner, N. Simonović, B. Solleder, J. Burgdörfer, L. Wirtz, Rumpling of LiF(001) surface from fast atom diffraction, Phys. Rev. A 82 (2010) 062902.

[41] J. Seifert, A. Schüller, H. Winter, K. Gärtner, Transition from axial to planar surface channeling for fast atom diffraction, Nucl. Instrum. Methods Phys. Res. B 269 (2011) 1212–1215.

[42] A.J. Garća, J.E. Miraglia, Total electron yields and stopping power of protons colliding with NaCl-type insulator surfaces, Phys. Rev. A 75 (2007) 042904.

[43] A. Momeni, P. Soulisse, P. Rousseau, H. Khemliche, P. Roncin, Grazing incidence fast atom diffraction (GIFAD): doing RHEED with ATOMS, e-J, Surf. Sci. Nanotech. 8 (2010) 101–104.

[44] J.R. Manson, H. Khemliche, P. Roncin, Theory of grazing incidence diffraction of fast atoms and molecules from surfaces, Phys. Rev. B 78 (2008) 155408.

[45] J.E. Miraglia, M.S. Gravielle, Reexamination of the interaction of atoms with a LiF (001) surface, Phys. Rev. A 95 (2017) 022710.

[46] M. Gravielle, J.E. Miraglia, Influence of the polarization in grazing scattering of fast helium atoms from LiF(001) Surfaces, Phys. Rev. A 78 (2008) 022901.

[47] H. Winter, Fast atom diffraction IBA in the regime of quantum scattering, Nucl. Instrum. Methods Phys. Res. B 332 (2014) 195–201.

[48] J. Seifert, H. Winter, Young-type Interference for scattering of fast Helium atoms from an Oxygen covered Mo(112) surface, Phys. Rev. Lett. 108 (2012) 065503.